Ion Dynamics and Nanostructures of Diluted Ionic Liquid Electrolytes

THE JOURNAL OF PHYSICAL CHEMISTRY C
A JOURNAL OF THE AMERICAN CHEMICAL SOCIETY

pubs.acs.org/JPCC

Article

Ion Dynamics and Nanostructures of Diluted Ionic Liquid Electrolytes

Filippa Lundin, Alexander Idström, Péter Falus, Lars Evenäs, Shizhao Xiong, and Aleksandar Matic*

Cite This: J. Phys. Chem. C 2022, 126, 16262−16271

Read Online

ACCESS | Metrics & More | Article Recommendations | Supporting Information

ABSTRACT: Diluted ionic liquid electrolytes are promising candidates in next-generation batteries enabling the implementation of lithium metal anodes. The diluent should fully mix with the ionic liquid while not interacting with the Li ions to preserve the ionic liquid character, which is beneficial for Li-metal electrode stability. We report on the influence of a hydrofluoroether (HFE) diluent on ion dynamics and nanostructure of an ionic liquid electrolyte. We show that the ionic liquid and the diluent are fully miscible and that the solvation structure of the Li ions is not affected by the presence of HFE. The increase in the conductivity by the addition of the diluent is directly related to a decrease in viscosity with faster dynamics of all ionic species. However, the relative increase in mobility is considerably larger for the ionic liquid cation as a result of a preferred interaction with HFE. On the microscopic scale, more complex local non-Gaussian diffusive dynamics are found, faster than what is expected from the self-diffusion coefficient. The relative change of the dynamics with the addition of HFE on macro- and microscopic length scales correlates well, which underlines the connection between the motions probed on different length and time scales.

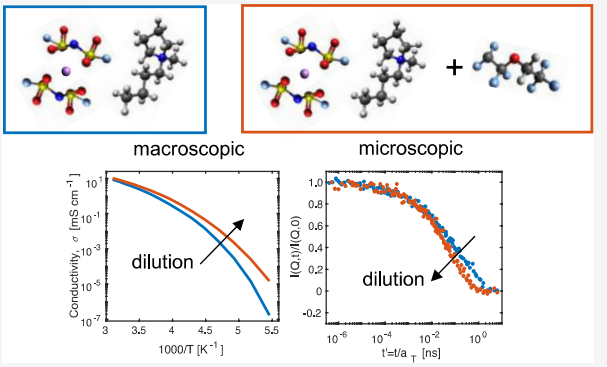

1. INTRODUCTION

There is currently a rapid development of next-generation electrochemical energy storage systems aiming to improve capacity, safety, and sustainability with respect to the state-of-the-art Li-ion technology. In particular, introducing lithium (Li) metal as the anode instead of graphite is an important route to increase the energy density of current battery systems based on intercalation chemistries. It is also a prerequisite for realization of the full potential of new conversion chemistries (such as Li−S or Li−O_2) where the very high capacity of the cathode needs to be matched at the anode side.[1] However, plating and stripping of Li during cycling in the commercial carbonate electrolyte result in a dendritic and mossy morphology with the formation of dead lithium and safety concerns if Li dendrites penetrate the separator.[2,3] In addition, the solid electrolyte interphase (SEI) on Li metal formed in carbonate-based electrolytes is unstable, leading to a continuous consumption of the electrolyte and active Li. Thus, developing new electrolytes that are safe, form a stable SEI, and prevent Li dendrite growth is of high importance to realize Li-metal batteries.

Ionic liquid electrolytes (ILEs), where a Li salt is dissolved in an ionic liquid, are regarded as safe electrolytes for battery application due to the characteristic properties such as a wide electrochemical stability window, high thermal stability, nonflammability, and low vapor pressure.[4,5] Adding a high concentration of Li salt to the ionic liquid has shown to increase the Li transference number, form a stable SEI on Li metal, suppress Li dendrite growth, and promote the rate capability of Li-metal batteries.[6−8] However, with increasing Li-salt concentration, the viscosity increases and the ionic conductivity decreases, and the wettability of separators and electrodes is often poor. A strategy to address these issues is to add a diluent to the electrolyte. The diluent must fully mix with the electrolyte (no phase separation) while not interacting with the Li ions to preserve their solvation structure, as well as have a low viscosity and be stable toward other cell components.[9]

One class of solvents that have been found to work well as diluents for highly concentrated electrolytes is hydrofluoroethers (HFEs). HFE has been used as a diluent in highly concentrated dimethoxyethane (DME)-based electrolytes with both lithium bis(fluorosulfonyl)imide (LiFSI) and potassium bis(fluorosulfonyl)imide (KFSI) salts resulting in the formation of stable SEIs on metal anodes.[10,11] Also, solvated ionic liquid electrolytes have successfully been diluted with HFEs. Dokko et al. showed that the Li-solvate structure in a glyme-based solvate ionic liquid remains intact upon the addition of

Received: June 28, 2022
Revised: September 4, 2022
Published: September 15, 2022

https://doi.org/10.1021/acs.jpcc.2c04503
J. Phys. Chem. C 2022, 126, 16262−16271

HFE.[12] This was further supported by Lu et al. who additionally showed that the performance of a Li−S cell is improved when HFE is added to a solvated ionic liquid electrolyte but also that at high HFE concentration the performance decreases as the solvation structure is affected.[13] For ionic liquid electrolytes, it has been shown that the addition of HFE increases conductivity, maintains the low flammability, creates a stable SEI on Li metal, and improves cycle life.[14−17] While these results are promising and point to a way to tailor ionic liquid-based electrolytes and other highly concentrated electrolytes, there is still a lack of microscopic understanding of the effect of dilution on the nanostructure and ion transport mechanism in these systems.

In this work, we investigate the microscopic structure and ion dynamics in HFE-diluted ionic liquid electrolytes as a function of HFE concentration. The chemical structure of the anion and cation of the ionic liquid and the HFE diluent used in this work are shown in Scheme 1. Previous studies have to a large extent focused on the macroscopic properties such as conductivity and cycling performance; here, we link this behavior to the local structure revealed by Raman spectroscopy and small-angle X-ray scattering (SAXS) and local dynamics investigated by quasi-elastic neutron scattering spectroscopy (QENS) and nuclear magnetic resonance (NMR) diffusometry. QENS is particularly suitable for investigating local dynamics and its relation to the nanostructure as it covers the typical time scales and length scales found in the ionic liquids,[18−23] whereas the chemical selectivity of NMR has the ability to distinguish the diffusion of Li, HFE, and the ionic liquid anion and cation.

Scheme 1. Chemical Structure of P14 Cation, FSI Anion, and HFE

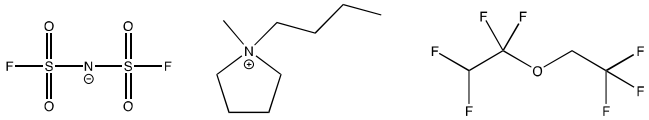

2. EXPERIMENTAL SECTION

2.1. Materials. 1-Butyl-1-methylpyrrolidinium bis(fluorosulfonyl)imide (P14FSI) from Solvionic (99.9%) and lithium bis(fluorosulfonyl)imide (LiFSI) from Suzhou Fluolyte (>99.5%) were mixed with 1,1,2,2-tetrafluoroethyl 2,2,2-trifluoroethyl ether (HFE) from DoDoChem (99.5%) in molar ratios: 1P14FSI/0.2LiFSI/xHFE, x = 0, 0.1, 0.5, and 1. For the QENS experiment, P14FSI from Solvionic (99.9%), LiFSI from Solvionic (99.9% <20 ppm H_2O), and 1,1,2,2-tetrafluoroethyl 2,2,2-trifluoroethyl ether (HFE) from TCI (>99.0%) were used and mixed in molar ratios: 1P14FSI/0.2LiFSI/xHFE with x = 0, 0.5, and 1. All samples were prepared and handled in an inert atmosphere.

2.2. Electrochemical Measurements. Cycling stability was evaluated in symmetric Li/Li-cells (Li disks, 10 mm diameter, and 200 μm thickness) with ILE and ILE/1HFE electrolytes and a glass fiber separator for current densities from 0.05 to 0.5 mAcm^{-2}.

2.3. Physical Characterization. Differential scanning calorimetry measurements were performed on a TA Instruments DSC 250. Samples were filled and sealed in hermetic aluminum pans in an argon-filled glovebox. DSC traces were recorded during heating from 113 to 313 K at a rate of 10 K/min. The glass transition was defined as the midpoint of the step in the DSC curve. Conductivity measurements were performed on a Novocontrol Broadband Dielectric Spectrometer in a frequency range of 10^{-2}−10^{7} Hz at a temperature range of 173−323 K. Stainless steel electrodes were separated by a 1 mm thick PEEK spacer. The DC conductivity was determined from the plateau value of the frequency-dependent conductivity. Density was measured using an Anton Paar DMA 4500 M oscillation U-tube densitometer at 289−339 K in steps of 10 K. A Lovis 2000 ME rolling ball viscometer module was used to determine the viscosities at the same temperatures as for the density.

To determine the self-diffusion coefficients, NMR experiments were performed using an AVANCE III HD Bruker NMR spectrometer, operating at 14.1 T and equipped with a Diff30 probe connected to a 60 A gradient amplifier. RF coil inserts of a 5 mm ^{1}H/^{2}H double coil, a 5 mm ^{19}F single coil, and a 5 mm ^{7}Li single coil configuration were used. The detailed experimental protocol is found in the Supporting Information. Specific NMR signals were used to follow the signal intensity attenuation of each species: the cation P14 was studied at 2.2 ppm in the ^{1}H spectrum, FSI at 51.8 ppm in the ^{19}F spectrum, HFE at 5.9 and −93.4 ppm for ^{1}H and ^{19}F, respectively, and Li at −0.9 ppm in the ^{7}Li-spectrum. Self-diffusion coefficients were determined at five temperatures in the range of 256−333 K (including 298 K) for ILE/1HFE and at 298 K for all other samples. All temperatures were calibrated using chemical shift differences in pure methanol or pure ethylene glycol prior to, and after, the experiments. Samples were filled in 5 mm NMR tubes and sealed in a glovebox.

Raman spectroscopy was performed on a Bruker MultiRAM Fourier transform Raman spectrometer equipped with a Nd:YAG laser (1064 nm) and a liquid nitrogen-cooled Ge-diode detector. The nominal laser power was 400 mW, the resolution was set to 1 cm^{-1} (full width at half-maximum), the Blackman−Harris three-term window function was used for apodization, and spectra were obtained as the average over 4000 scans. Fitting of spectra was performed with the PeakFit software package, using a linear background and Voigt profiles.

Small-angle X-ray scattering experiments were performed on a SAXSLAB Mat:Nordic with a Rigaku 003+ high brilliance microfocus Cu-radiation source and a Pilatus 300 K detector. The data was collected in a single measurement using the WAXS setting covering a Q-range of 0.1−2.2 Å^{-1}. Each sample was measured for 30 minutes in a 1.5 mm diameter glass capillary (sealed with wax in an inert atmosphere) at room temperature. No background sample cell background measurement was needed since the capillaries have a very weak contribution in the measured region.

Neutron spin-echo spectroscopy (NSE) was performed on a WASP spectrometer, Institute Laue-Langevin (ILL), France.[24] The momentum transfer is determined by the wavelength of the neutrons and the detector angle according to

$$Q = \frac{4\pi}{\lambda}\sin\left(\frac{\theta}{2}\right) \quad (1)$$

The time window covered by the spectrometer depends on the incident neutron wavelength, with shorter time scales being probed for shorter incident wavelengths. In our experiment, a wavelength of 7 Å and a detector angle of 70° were used, resulting in a time window of 6 ps to 6 ns and a momentum

https://doi.org/10.1021/acs.jpcc.2c04503
J. Phys. Chem. C 2022, 126, 16262−16271

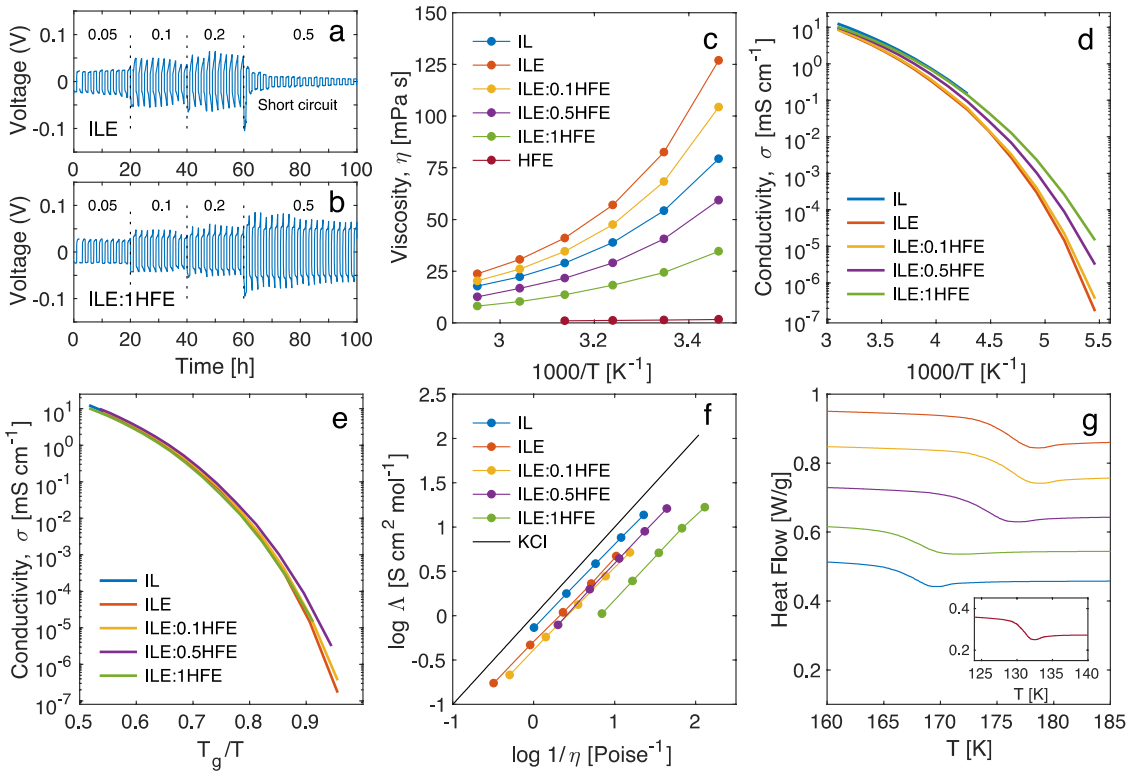

Figure 1. Voltage profiles of LilLi symmetric cells with (a) ionic liquid electrolyte and (b) HFE-diluted ionic liquid electrolyte at current densities of 0.05, 0.1, 0.2, and 0.5 mAcm^{-2}. Arrhenius plot of (c) viscosity and (d) ionic conductivity, (e) T_g-scaled Arrhenius plot of ionic conductivity, (f) Walden plot, and (g) DSC traces from heating scans for ionic liquid, ionic liquid electrolytes, and HFE (inset). Data has been vertically offset for clarity.

transfer range of Q = 0.6−1.5 Å^{-1}. Data was collected in the temperature range of 180−300 K, and the measurement time was 4 h for each temperature. A measurement of P14FSI/0.2LiFSI at 50 K was used as a resolution, and an empty cell was used for background subtraction. Data was subsequently normalized to a measurement from a fully elastically scattering TiZr sample. Annular TiZr cans, sample thickness of 0.2 mm, were used as sample holders. The data was reduced using ILL-developed routines implemented in Igor Pro 8.[25]

3. RESULTS AND DISCUSSION

The ionic liquid electrolyte is formed by the mixture of the ionic liquid P14FSI and the salt LiFSI. FSI-based ionic liquids have previously been shown to improve the cyclability of Li-metal anodes; however, their rather viscous nature reduces their performance at higher current densities. Figure 1a,b compares the stripping/plating of lithium in the ionic liquid electrolyte and the diluted ionic liquid electrolyte (ILE/1HFE) at different current densities. For the ionic liquid electrolyte, stable voltage profiles are observed up to 0.2 mAcm^{-2}, which shows that a stable interface is formed on the Li-metal electrode during plating/stripping. However, for the highest current density, 0.5 mAcm^{-2}, the voltage drops as a result of an internal short-circuit related to the fast growth of Li dendrites at higher current densities.[26] In contrast, the cell with the diluted IL electrolyte maintains a stable voltage profile also at a high current density and overall the overvoltage is also slightly lower for the diluted electrolyte. Thus, the addition of HFE leads to an overall lower cell resistance, originating from both interfacial resistance and the resistance of the bulk electrolyte, and decreases the growth rate of Li dendrites.[17]

The improvement of the performance with the addition of HFE can be traced back to the physical properties of the electrolytes. Figure 1c,d shows the viscosity and conductivity of the ionic liquid electrolytes, the neat ionic liquid (P14FSI), and the diluent (HFE). Adding the Li salt (LiFSI) to the IL increases the viscosity and lowers the conductivity, while the addition of HFE decreases the viscosity and increases the conductivity, in agreement with previous studies.[16,17,27] The temperature dependencies of the viscosity and the conductivity follow the Vogel−Fulcher−Tamman (VTF) relation, commonly found for liquids, and fits of the data to the VFT equation (eq S3) are found in Figures S1 and S2 and the parameters are reported in Tables S1 and S2. Transport properties of ionic liquids are closely related to the glass-transition temperature (T_g).[28] The T_g, determined by DSC, is shown in Figure 1g and Table S3. T_g increases with the addition of salt, which agrees well with previous studies.[27,29] Adding HFE, which has a much lower T_g than the ILE, lowers T_g of the mixtures. Figure 1e shows a T_g-scaled Arrhenius plot of the conductivity, where a master curve is expected if only the viscosities of the electrolytes are responsible for the changes in the conductivity with composition. However, even though there is a partial overlap of the curves in Figure 1e, a deviation from a master curve can be seen for low temperatures (high T_g/T). This implies that there are also additional changes not accounted for by the glass-transition temperature upon the introduction of HFE, such as changes in local structure, interactions, and/or effective number of charge carriers. To further shed light on this issue, Figure 1f shows Walden plots for the IL and ILEs obtained from the viscosity,

https://doi.org/10.1021/acs.jpcc.2c04503
J. Phys. Chem. C 2022, 126, 16262−16271

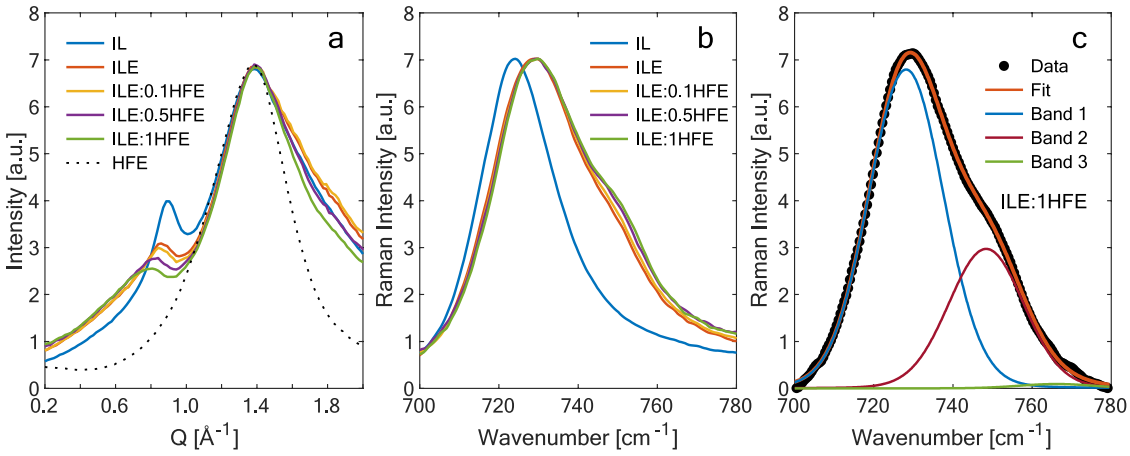

Figure 2. SAXS patterns (a) and Raman spectra (b) for IL and ILEs. Intensity in SAXS and Raman data is normalized to the maximum peak intensity. (c) Example of the deconvoluted Raman spectrum of ILE/1HFE and the resulting fit (see the text).

ionic conductivity, and density data (see Figure S3). Walden plots were obtained using

$$\log\ \Lambda = \log c + \alpha \log\left(\frac{1}{\eta}\right) \tag{2}$$

where Λ is the molar conductivity (conductivity/molar concentration) [Scm^2 mol^{-1}], c and α are constants, and η is the viscosity. Densities used to calculate the molar conductivities are found in Figure S3. It provides a measure of the ionicity of a liquid, and the KCl line represents a solution where ions are fully dissociated and the ion transport follows the viscous behavior. Below that line, the ionicity decreases as a result of increased ion interactions.[30,31] Adding a Li salt to the ionic liquid has previously been shown to result in a slight decrease in the ionicity,[29,32] and our results are in agreement with this. With the addition of HFE, there is basically no change in the ionicity for lower HFE concentrations (up to ILE/0.5HFE). A similar behavior was also seen by Liu et al.[16] However, for high diluent concentration (ILE/1HFE), a larger change in the Walden plot is observed, which shows that the increase in the overall conductivity is lower than the increase in viscosity.

3.1. Nanostructure and Li-Ion Interactions. A hallmark of ionic liquids is a nanoscale structure related to charge ordering and the formation of apolar domains.[33] It is a result of the competition of van der Waals and Coulomb interactions and is manifested by the presence of a well-defined peak located at a few nm^{-1} in the static structure factor, probed by, for instance, SAXS. Figure 2a shows the SAXS patterns from the IL-based electrolytes together with the neat ionic liquid and HFE for comparison. For HFE, only the molecular peak at 1.4 Å^{-1}, related to the nearest-neighbor distance, can be observed, indicative of the lack of correlations beyond the nearest neighbors in simple liquids. In the ionic liquid, in agreement with previous studies,[33] an additional peak at 0.9 Å^{-1} related to charge ordering is found, i.e., from the correlation of ions of the same charge (cation−cation and anion−anion). With the addition of the lithium salt (LiFSI), the charge ordering peak decreases in intensity and shifts to lower Q, in agreement with previous results on similar ionic liquids,[16,34] whereas the position of the main peak at 1.4 Å^{-1} does not change. This behavior has been correlated to the presence of LiFSI clusters (e.g., Li[FSI]$_x$$x$ = 2 or 3) forming a larger effective anion;[35] thus, the overall charge alternation distance increases and the peak in the structure factor shifts to lower Q.[34] With the addition of HFE, there is a further shift of the charge ordering peak to lower Q, indicating a further increase in the average charge alternation distance. This shows that HFE somewhat influences the nanoscale structure of the IL electrolyte, causing a further separation of similar charges. A scenario that is compatible with this observation is that HFE does not interact with the Li[FSI]$_x$ clusters but is preferentially associated with the P14 cation of the ionic liquid and in this way effectively increases the length scale of charge ordering. Figure S4 shows the SAXS pattern from ILE and IL/1HFE showing that adding HFE to the neat IL also influences the charge ordering in a similar way to adding salt, however, with the shift being related to the ordering of P14 and HFE rather than the FSI and Li. One should also note that there are no features in the SAXS at low Q with the addition of HFE, which would indicate a phase-separated structure with larger HFE domains. Thus, the HFE is fully dispersed in the ionic structure of the IL.

To further investigate the local coordination of Li ions, Raman spectroscopy was performed. Full Raman spectra of the IL-based electrolytes are found in Figure S5. Figure 2b shows the normalized Raman spectra of the ILEs and the IL for comparison in the region 700−780 cm^{-1} where the band originating from the symmetric stretching of the FSI ion is found. This band has previously been used to account for FSI ions that are free or coordinated to Li$^+$ in ionic liquids.[35] With the addition of Li salt, the band shifts to higher wavenumbers and a new band also appears as a shoulder on the high-frequency flank, attributed to FSI coordinated to Li$^+$. With the addition of HFE, there are only small changes to the band profiles, with a slight increase in the intensity of the high-frequency shoulder with increasing HFE concentration. This indicates that we can expect that the local Li-ion environment is preserved when the diluent is added.

To quantitatively analyze the LiFSI coordination, the Raman spectra in the 700−780 cm^{-1} region have been deconvoluted into three bands (Figure 2c), where the two main components correspond to the free (lower-frequency component) and coordinated (higher-frequency component) FSI, respectively. The weak third component, found in the high-frequency tail of the region, is related to the IL cation[35,36] and is found to decrease with the addition of HFE. Using the areas of the

https://doi.org/10.1021/acs.jpcc.2c04503
J. Phys. Chem. C 2022, 126, 16262−16271

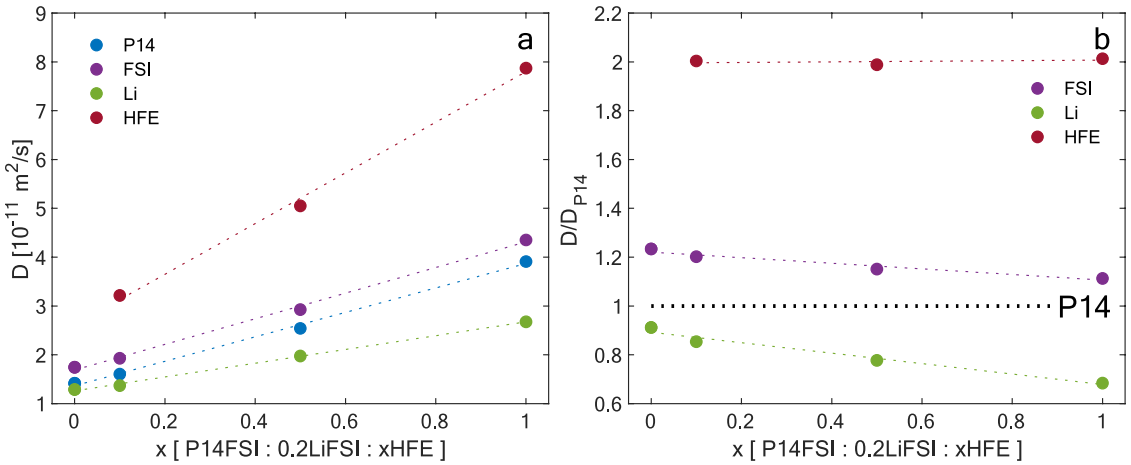

Figure 3. (a) Self-diffusion coefficients (D) of the components of IL-based electrolytes at 297 K determined from pulsed-field gradient NMR spectroscopy. (b) Ratio between the self-diffusion coefficients of the components of the electrolytes and the self-diffusion coefficient of the P14 cation. Errors bars are within the size of the symbols. Dotted lines are guides to the eye.

bands corresponding to the free (A_1, low-frequency component) and Li-ion-coordinated (A_2, high-frequency component) FSI ions, the fraction of lithium-coordinated FSI ions, C_{coord}, can be calculated from eq 3[37]

$$C_{coord} = \frac{A_2}{A_1 + A_2} \tag{3}$$

From the fraction of coordinated FSI ions, one can calculate the average number of FSI interacting with each Li^+ from

$$N_{FSI/Li} = \frac{C_{coord}}{x} \tag{4}$$

where x is the molar fraction of Li^+ with respect to FSI. The results from the band deconvolution and the calculation of $N_{FSI/Li}$ can be found in Table S4. The value of $N_{FSI/Li}$ is close to 2, in agreement with previous results, and a very slight increase in the band positions and $N_{FSI/Li}$ is observed with the addition of HFE. Thus, this shows that the HFE successfully dilutes the ILE without interrupting the solvation structure of Li ions, pointing to a preferential interaction of HFE with the cation, as also inferred from the SAXS results.

3.2. Ion Dynamics. With NMR diffusometry, the dynamics of the different species in the IL-based electrolytes can be selectively probed. Using ^1H, ^7Li, and ^{19}F resonances, and taking into account the specific chemical shifts, the self-diffusion coefficients for the P14 cation, the FSI anion, Li^+, and HFE can be determined (see the Experimental Section). All NMR signals obeyed a strict single-exponential attenuation of the intensity versus squared pulsed-field gradient strength. This pattern was omnipresent in the entire range of selected experimental diffusion times from 25 ms to 400 ms and investigated temperatures. Hence, there is no indication of a multiphase system but rather the typical behavior of a one-phase liquid.

Figure 3a shows the self-diffusion coefficients (D) at 298 K for the components of the ionic liquid electrolytes as a function of HFE concentration. In the neat ionic liquid electrolyte, the FSI shows the fastest translational dynamics and Li^+ the slowest, in agreement with the previous work.[38] For neat HFE, the dynamics are much faster than in the IL electrolyte, the self-diffusion coefficient of HFE being more than 50 times higher (see Table S5).

With the addition of HFE, the dynamics in the diluted electrolytes get progressively faster and the self-diffusion coefficients for all ions increase. The trend between the ions is preserved with the FSI anion being the fastest and Li^+ the slowest, but the highest self-diffusion coefficient is found for HFE, which is about a factor of 2 higher than for the ionic components. However, comparing the increase in self-diffusion coefficient with HFE concentration for the species of the IL electrolyte, it is clear that the influence on their dynamics is different (see Figure S6). In Figure 3b, the self-diffusion coefficients for different HFE concentrations are normalized to the self-diffusion coefficient of the P14 cation. It is evident that with the addition of HFE the increase in the diffusion coefficients of Li^+ and FSI is lower compared to the increase in D_{P14} and D_{HFE}. In fact, the dynamics of the P14 cation and HFE are strongly correlated, implying that the HFE interacts preferentially with P14 rather than with FSI and Li^+. This is fully in line with previous suggestions that the interaction between the Li^+ and HFE/cation is weak,[17] which, in turn, is in strong agreement with our results from Raman spectroscopy that the local coordination of Li^+ is preserved. The difference in the increase of the diffusion coefficient for different ionic species can explain the change in the Walden plot at high HFE concentrations (see above). While the P14 cation and HFE basically follow the behavior of the viscosity, the dynamics of Li^+ and FSI are influenced much less, lowering the overall increase in the conductivity. Thus, the effect observed in the Walden plot is not directly a change in ion interactions but rather a change in the contribution of the different species to the total conductivity.

To track the dynamics on the microscopic scale, neutron spin-echo spectroscopy (NSE) was applied. In an NSE experiment, the intermediate scattering function provides information on dynamics on ps−ns time scales and on length scales corresponding to the nanostructure of the ionic liquid (6 ps to 6 ns and momentum transfers 0.6−1.5 $Å^{-1}$ in our experiment). In a material where the incoherent scattering dominates, the NSE probes the self-correlations, such as self-diffusion.[39] Thus, the results can be directly compared to the dynamics probed on macroscopic length scales by NMR. In the ILEs, the scattering is >90% incoherent due to the strong contribution of the H-atoms to the P14 cation (see Tables S6

https://doi.org/10.1021/acs.jpcc.2c04503
J. Phys. Chem. C 2022, 126, 16262−16271

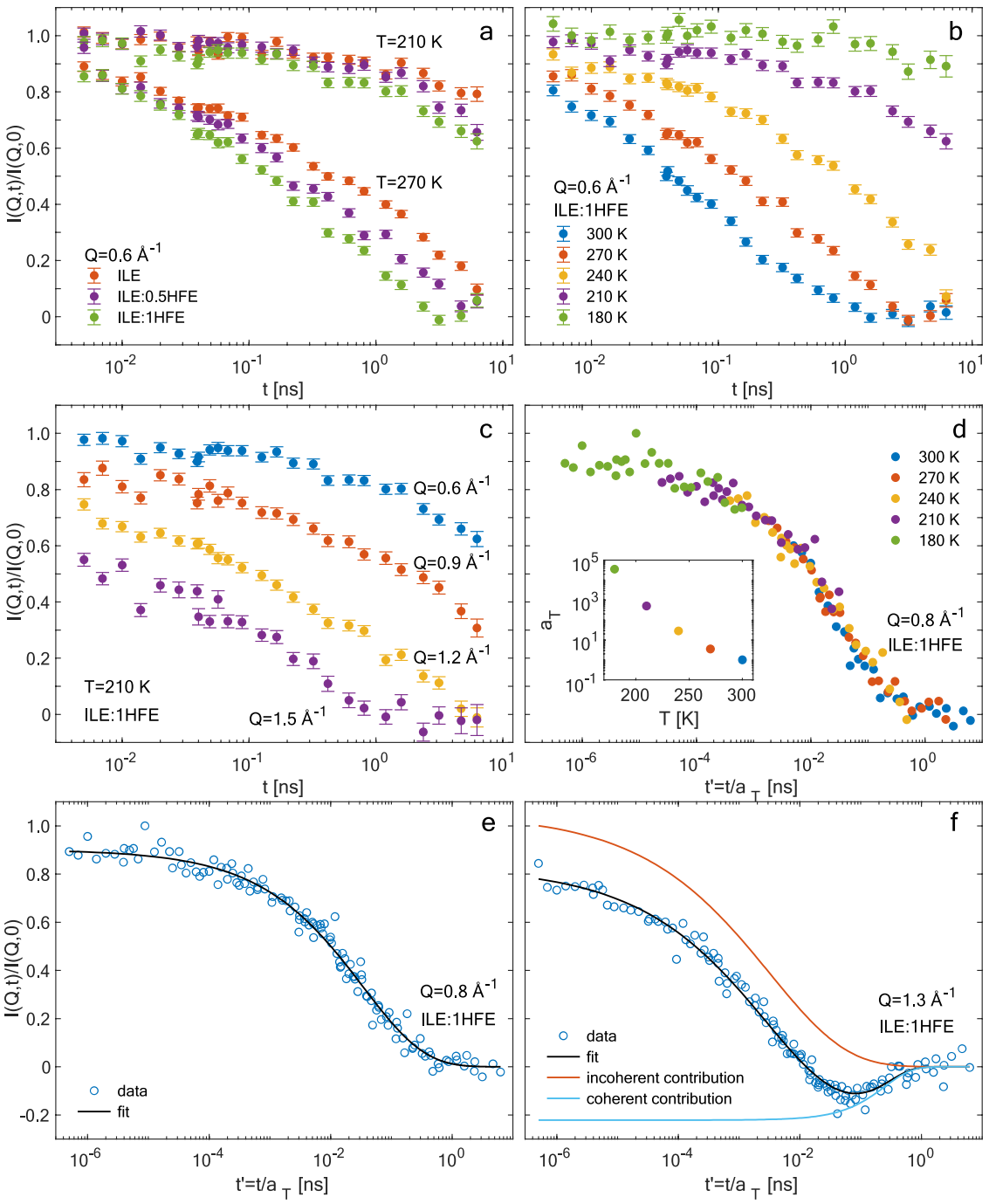

Figure 4. Intermediate scattering functions of (a) ILEs with different HFE concentrations and at two temperatures at $Q = 0.6$ Å^{-1}. (b) ILE/1HFE at $Q = 0.6$ Å^{-1} as a function of temperature. (c) Intermediate scattering function of ILE/1HFE as a function of momentum transfer at 210 K. (d) Time−temperature superposition of the intermediate scattering function of ILE/1HFE at $Q = 0.8$ Å^{-1}. The inset shows the shift parameter (a_T) as a function of temperature. Examples of fits to the TTS curves of ILE/1HFE (e) at $Q = 0.8$ Å^{-1} fitted with only an incoherent contribution and (f) at $Q = 1.3$ Å^{-1} fitted with one incoherent and one coherent contributions.

and S7 in the Supporting Information); thus, the NSE experiment mainly probes the dynamics of the P14 cation.

Figure 4a shows intermediate scattering functions, $I(Q,t)$, from the NSE experiment for ILEs with different HFE concentrations at two temperatures, and Figure 4b shows the function of temperature for the highest HFE concentration. As expected, the dynamics become slightly faster with increasing HFE concentration and show strong temperature dependence. In the time window of the spectrometer, the system goes from non- to fully relaxed when the temperature is increased from 180 K, i.e., close to the glass-transition temperature ($T_g = 167$ K), where $I(Q,t)/I(Q,0) \approx 1$, to room temperature, where $I(Q,t)/I(Q,0)$ reaches zero. Figure 4c shows the intermediate scattering function for ILE/1HFE at 210 K at different momentum transfers (Q). With increasing Q, the dynamics become faster, i.e., the scattering curves are progressively shifted to shorter time scales. This Q-dependence is indicative of dynamics of diffusive origin.[39]

To further investigate the temperature dependence of the intermediate scattering functions, we performed a time−

https://doi.org/10.1021/acs.jpcc.2c04503
J. Phys. Chem. C 2022, 126, 16262−16271

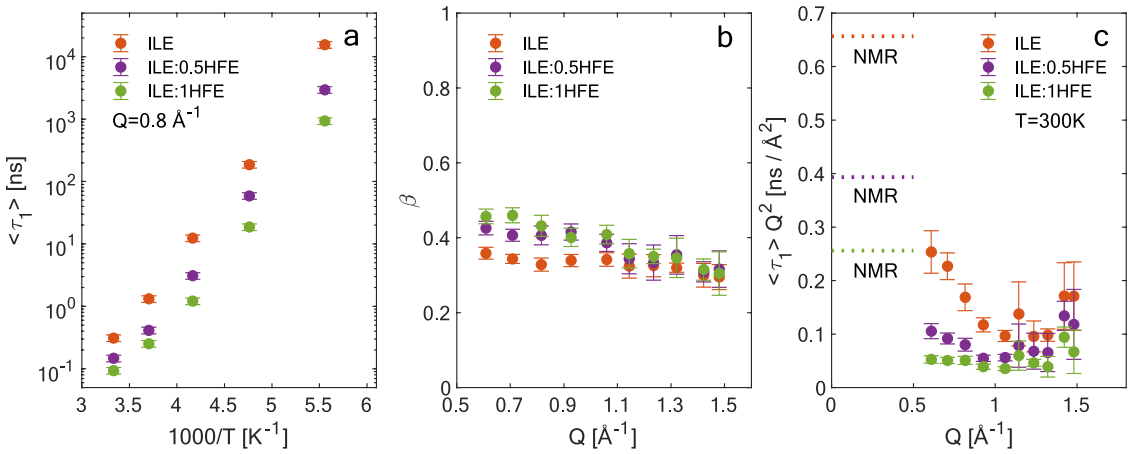

Figure 5. (a) Mean relaxation time for ILEs at Q = 0.8 Å^{-1} as a function of inverse temperature. (b) Stretching parameter β for the different concentrations at 300 K. (c) Momentum transfer dependence of the average relaxation time multiplied with Q^2 as a function of HFE concentration at 300 K.

temperature superposition (TTS) analysis. A TTS analysis can reveal if the temperature dependence only shifts the relaxation function in time, i.e., the overall shape is preserved, or if additional processes enter the time window of the spectrometer as the temperature is increased. In the case of an invariant shape of the scattering function as a function of temperature, a master curve can be constructed by introducing $t' = t/a_T$, where the a_T(T) is a shift factor chosen to provide the best overlap between the scattering curves recorded at different temperatures. Figure 4d shows an example of a TTS analysis, and TTS curves for all investigated samples are shown in the Supporting Information (Figures S11−S13). Shift factors used to construct the TTS curves, a_T, are found in Figures S7 and S8, respectively, and qualitatively follow the temperature dependence of the viscosity (Figure S9). The large overlap of the data for different temperatures made it possible to superposition all of the scattering curves into a master curve for each composition, without any other scaling of the data. This shows that the shape of the scattering curve is invariant with temperature and just shifted within the experimental window of the spectrometer. Thus, in the experiment, we in fact probe different parts of the same relaxation function for different temperatures. Overall, the TTS curves show only one major relaxation. However, for momentum transfers Q > 1.1 Å^{-1}, the scattering function goes negative (for all concentrations). This is a result of the normalization of the neutron spin-echo signal by the neutron polarization in the case of a dominantly incoherent signal. Since only around 10% of the scattering is coherent, the effect is rather weak and only shows up around the peak for the static structure factor (1.4 Å^{-1}) where the coherent scattering is the strongest and the incoherent contribution is low (end of relaxation function) (Figure 4e,f).

To extract the relaxation time as a function of temperature, the TTS curves were fitted, and the shift factors were subsequently used to obtain the relaxation time at each temperature. For Q < 1.1 Å^{-1}, where only the incoherent contribution is present, a stretched exponential function was used to account for the relaxation (eq 5 and Figure 4e), whereas for Q > 1.1 Å^{-1} an additional single-exponential contribution was introduced to account for the coherent contribution (eq 6 and Figure 4f), where $\tau_{1,2}$ are the relaxation times, β is the stretching parameter, and A and B are the scattering amplitudes of the two relaxations

$$\frac{I(Q,t)}{I(Q,0)} = A\cdot e^{-\left(\frac{t}{\tau_1}\right)^{\beta}} \quad Q < 1.1\ \text{Å}^{-1} \tag{5}$$

$$\frac{I(Q,t)}{I(Q,0)} = A\cdot e^{-\left(\frac{t}{\tau_1}\right)^{\beta}} - B\cdot e^{-\left(\frac{t}{\tau_2}\right)} \quad Q > 1.1\ \text{Å}^{-1} \tag{6}$$

Figure 5 shows the results from fits of the TTS curves of the main (incoherent) relaxation process (fitting parameters A and B are found in Figure S10). All fits and the results for the coherent process are found in Figures S11−S14 in the Supporting Information. The ratio of the coherent to the incoherent contributions (B/A) from the fit to eq 6 follows what one can expect for the coherent and incoherent scattering from the polarization measurements in the experiment, where the coherent contribution is around 20% of the coherent one at the higher momentum transfers where it is the strongest. The mean relaxation time (Figure 5a), taking the stretching exponent into account, is calculated as

$$\langle\tau_1\rangle = \Gamma\left(\frac{1}{\beta}\right)\cdot\frac{1}{\beta}\cdot\tau_1 \tag{7}$$

where Γ is the gamma function.[39] The stretching parameter β is around 0.4 (see Figure 5b), and it is similar for the ILEs with different HFE concentrations. The low β value indicates that the dynamics are heterogeneous, i.e., a distribution of relaxation times, or of a more cooperative nature.[39] Similar values of β have previously been reported for a neat ionic liquid,[40] and here we show that the addition of the diluent does not dramatically affect the nature of the dynamics. The mean relaxation time (Figure 5a) shows a strong temperature dependence, and the local IL cation dynamics are faster with increasing HFE concentration, in agreement with the faster macroscopic dynamics.

The momentum transfer dependence of the mean relaxation time, $\langle\tau_1\rangle$, gives information about the nature of the motion where a decrease with momentum transfer is a signature of diffusive dynamics, whereas local/internal processes usually show a Q-independent relaxation time and also occur at faster time scales.[23] For a Fickian diffusion process, $\langle\tau_1\rangle \propto Q^{-2}$ is expected.[39] In Figure 5c, the momentum transfer dependence

https://doi.org/10.1021/acs.jpcc.2c04503
J. Phys. Chem. C 2022, 126, 16262−16271

of the average relaxation time multiplied with Q^2 is shown for the main relaxation process in the ILEs to highlight where we can expect a Fickian behavior, and in Figure S15, $\langle\tau_1\rangle$ vs Q^2 is shown. The results clearly show that we do not observe simple Fickian diffusive dynamics for the P14 cation. At low momentum transfers, the momentum transfer dependence is in fact stronger than Q^2, whereas a transition to Q^2 is found around $Q \approx 1\text{Å}^{-1}$. One can also note that the dynamics are faster than what is extrapolated from the self-diffusion coefficient determined from NMR. This type of crossover behavior in the dynamics with momentum transfer has also been reported for a neat ionic liquid, where it was attributed to a transition from Gaussian to non-Gaussian behavior.[40] With the addition of HFE, the crossover becomes less pronounced, but the same trend is clearly observed. The coherent relaxation process occurs at slightly slower time scales, but overall, it shows a similar behavior as the incoherent process with respect to both temperature and momentum transfer dependencies (see Figure S14).

Figure 6 compares the relative change in the mean relaxation times from NSE, self-diffusion coefficients of the cation from

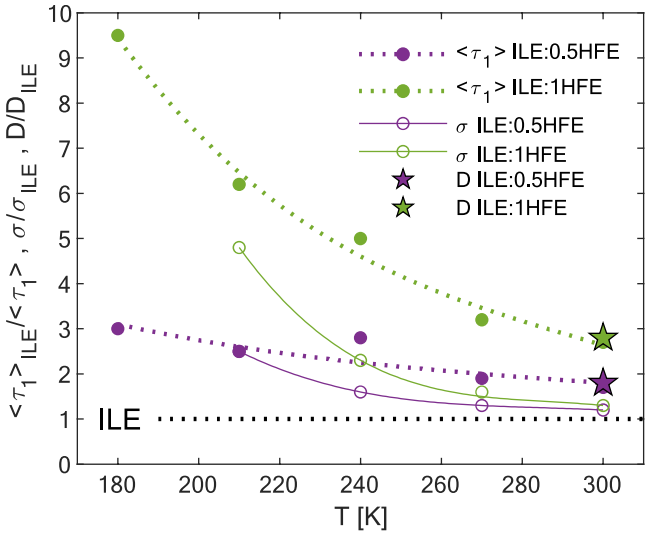

Figure 6. Relative change in the mean relaxation time, self-diffusion coefficient of the P14 cation, and conductivity with the addition of HFE.

NMR, and conductivity with the addition of HFE. There is a strong correlation in the relative change of D_{P14} and $\langle\tau_1\rangle$ with HFE concentration underlining the connection between these two processes. However, the relative change in the conductivity is lower, which is connected to the fact that here also the dynamics of Li^+ and FSI^- contribute and the effect of HFE on their dynamics is considerably smaller, as shown by the NMR results (see Figure 3). To further compare the dynamics at different length scales, the apparent activation energies around room temperature for $\langle\tau_1\rangle$ from NSE, D_{P14} from NMR, and conductivity are found in Table 1. The activation energies determined by the different techniques are similar, showing a direct connection between the processes on different length scales. One can also note a slight decrease in the activation energy with the addition of HFE.

CONCLUSIONS

The influence of the addition of HFE, as a diluent to an ionic liquid electrolyte, on the local structure and dynamics was studied. With the addition of HFE, the cyclability of Li-metal anodes is improved, especially at high current densities. This is related to the increased ionic conductivity and lowered viscosity of the electrolyte with the addition of HFE while preserving the characteristics of the ionic liquid electrolyte with the formation of a stable interface toward the Li metal. We show that the ionic liquid and the diluent are fully miscible forming a single-phase liquid. On the microscopic scale, the characteristic nanostructure with charge correlation in the ionic liquid is preserved as well as the local Li-ion environment. The improved conductivity of importance for the rate capability of the electrolyte is a result of an overall increase in ion dynamics, as observed from the self-diffusion coefficients determined by NMR. However, it is clear that the addition of HFE has a larger effect on the dynamics of the ionic liquid cation (P14) compared to Li^+ and the ionic liquid anion (FSI), pointing to a stronger interaction between HFE and P14, fully in line with the result that the local structure around Li^+ is preserved. On the microscopic scale, we reveal diffusive dynamics of the cation occurring on time scales faster than expected from the self-diffusion coefficient. Comparing the influence of the addition of HFE on the dynamics on different length scales shows that the addition of HFE has the same relative effect on the dynamics, underlining the connection between these two processes. The local dynamics show a cooperative and non-Gaussian behavior, typical for ionic liquid. With the addition of HFE, this behavior is still observed; however, the time scale for the local motion and the self-diffusion come closer together as a result of the interaction with HFE and the decoupling of the cation dynamics from that of the FSI anion and Li^+. Our results on the local structure and dynamics provide direct evidence of the role of HFE-type diluents on highly concentrated electrolytes, i.e., diluents that aim to improve the dynamics without sacrificing the beneficial properties of the base electrolyte.[10,11] We here show that this is provided by a preferential interaction between the diluent and the ionic liquid cation, whereas the local coordination of Li^+ is preserved, as previously also suggested for other highly concentrated electrolytes.[12]

ASSOCIATED CONTENT

Supporting Information

The Supporting Information is available free of charge at https://pubs.acs.org/doi/10.1021/acs.jpcc.2c04503.

NMR diffusometry method, glass-transition temperatures, density, SAXS pattern, Raman spectra, diffusion

Table 1. Activation Energies Calculated from NSE, NMR, and Conductivity for ILE with Different HFE Concentrations

HFE concentration	$E_{a\ NSE}$ (270−300 K)	$E_{a\ NMR}$ (275−297 K)	$E_{a\ \sigma}$ (273−303 K)
0 HFE	28 ± 3 kJ/mol		31 ± 3 kJ/mol
0.5 HFE	26 ± 3 kJ/mol		29 ± 3 kJ/mol
1 HFE	25 ± 2 kJ/mol	28 ± 2 kJ/mol	26 ± 3 kJ/mol

https://doi.org/10.1021/acs.jpcc.2c04503
J. Phys. Chem. C 2022, 126, 16262−16271

coefficients, neutron scattering, scaling parameter, and intermediate scattering functions (PDF)

AUTHOR INFORMATION

Corresponding Author

Aleksandar Matic − *Department of Physics, Chalmers University of Technology, Göteborg, SE 412 96, Sweden;* orcid.org/0000-0003-4414-9504; Phone: +46(0)31-7725176; Email: matic@chalmers.se

Authors

Filippa Lundin − *Department of Physics, Chalmers University of Technology, Göteborg, SE 412 96, Sweden*

Alexander Idström − *Department of Chemistry and Chemical Engineering, Chalmers University of Technology, Göteborg, SE 412 96, Sweden*

Péter Falus − *Institut Laue-Langevin, Grenoble 38042, France*

Lars Evenäs − *Department of Chemistry and Chemical Engineering, Chalmers University of Technology, Göteborg, SE 412 96, Sweden;* orcid.org/0000-0002-6580-0610

Shizhao Xiong − *Department of Physics, Chalmers University of Technology, Göteborg, SE 412 96, Sweden*

Complete contact information is available at: https://pubs.acs.org/10.1021/acs.jpcc.2c04503

Notes

The authors declare no competing financial interest.

ACKNOWLEDGMENTS

This research was financially supported by the Swedish Foundation for Strategic Research (SSF) within the Swedish National Graduate School in Neutron Scattering (SwedNess) grant number GSn15-0008.

REFERENCES

(1) Wang, R.; Cui, W.; Chu, F.; Wu, F. Lithium Metal Anodes: Present and Future. *J. Energy Chem.* **2020**, *48*, 145−159.

(2) Zhang, X.; Yang, Y.; Zhou, Z. Towards Practical Lithium-Metal Anodes. *Chem. Soc. Rev.* **2020**, *49*, 3040−3071.

(3) Yamada, Y.; Wang, J.; Ko, S.; Watanabe, E.; Yamada, A. Advances and Issues in Developing Salt-Concentrated Battery Electrolytes. *Nat. Energy* **2019**, *4*, 269−280.

(4) Matic, A.; Scrosati, B. Ionic Liquids for Energy Applications. *MRS Bull.* **2013**, *38*, 533−537.

(5) Jónsson, E. Ionic Liquids as Electrolytes for Energy Storage Applications − A Modelling Perspective. *Energy Storage Mater.* **2020**, *25*, 827−835.

(6) Sun, H.; Zhu, G.; Zhu, Y.; Lin, M.-C.; Chen, H.; Li, Y.-Y.; Hung, W. H.; Zhou, B.; Wang, X.; Bai, Y.; et al. High-Safety and High-Energy-Density Lithium Metal Batteries in a Novel Ionic-Liquid Electrolyte. *Adv. Mater.* **2020**, *32*, No. 2001741.

(7) Yoon, H.; Howlett, P. C.; Best, A. S.; Forsyth, M.; MacFarlane, D. R. Fast Charge/Discharge of Li Metal Batteries Using an Ionic Liquid Electrolyte. *J. Electrochem. Soc.* **2013**, *160*, A1629−A1637.

(8) Heist, A.; Lee, S.-H. Improved Stability and Rate Capability of Ionic Liquid Electrolyte with High Concentration of LiFSI. *J. Electrochem. Soc.* **2019**, *166*, A1860−A1866.

(9) Cao, X.; Jia, H.; Xu, W.; Zhang, J.-G. Review—Localized High-Concentration Electrolytes for Lithium Batteries. *J. Electrochem. Soc.* **2021**, *168*, No. 10522.

(10) Qin, L.; Xiao, N.; Zheng, J.; Lei, Y.; Zhai, D.; Wu, Y. Localized High-Concentration Electrolytes Boost Potassium Storage in High-Loading Graphite. *Adv. Energy Mater.* **2019**, *9*, No. 1902618.

(11) Ding, J.-F.; Xu, R.; Yao, N.; Chen, X.; Xiao, Y.; Yao, Y.-X.; Yan, C.; Xie, J.; Huang, J.-Q. Non-Solvating and Low-Dielectricity Cosolvent for Anion-Derived Solid Electrolyte Interphases in Lithium Metal Batteries. *Angew. Chem., Int. Ed.* **2021**, *60*, 11442−11447.

(12) Dokko, K.; Tachikawa, N.; Yamauchi, K.; Tsuchiya, M.; Yamazaki, A.; Takashima, E.; Park, J.-W.; Ueno, K.; Seki, S.; Serizawa, N.; Watanabe, M. Solvate Ionic Liquid Electrolyte for Li−S Batteries. *J. Electrochem. Soc.* **2013**, *160*, A1304−A1310.

(13) Lu, H.; Yuan, Y.; Hou, Z.; Lai, Y.; Zhang, K.; Liu, Y. Solvate Ionic Liquid Electrolyte with 1,1,2,2-Tetrafluoroethyl 2,2,2-Trifluoroethyl Ether as a Support Solvent for Advanced Lithium−Sulfur Batteries. *RSC Adv.* **2016**, *6*, 18186−18190.

(14) Fang, S.; Qu, L.; Luo, D.; Shen, S.; Yang, L.; Hirano, S. Novel Mixtures of Ether-Functionalized Ionic Liquids and Non-Flammable Methylperfluorobutylether as Safe Electrolytes for Lithium Metal Batteries. *RSC Adv.* **2015**, *5*, 33897−33904.

(15) Lu, H.; Chen, Z.; Du, H.; Zhang, K.; Wang, J.; Hou, Z.; Fang, J. The Enhanced Performance of Lithium Sulfur Battery with Ionic Liquid-Based Electrolyte Mixed with Fluorinated Ether. *Ionics* **2019**, *25*, 2685−2691.

(16) Liu, X.; Zarrabeitia, M.; Mariani, A.; Gao, X.; Schütz, H. M.; Fang, S.; Bizien, T.; Elia, G. A.; Passerini, S. Enhanced Li+ Transport in Ionic Liquid-Based Electrolytes Aided by Fluorinated Ethers for Highly Efficient Lithium Metal Batteries with Improved Rate Capability. *Small Methods* **2021**, *5*, No. 2100168.

(17) Wang, Z.; Zhang, F.; Sun, Y.; Zheng, L.; Shen, Y.; Fu, D.; Li, W.; Pan, A.; Wang, L.; Xu, J.; et al. Intrinsically Nonflammable Ionic Liquid-Based Localized Highly Concentrated Electrolytes Enable High-Performance Li-Metal Batteries. *Adv. Energy Mater.* **2021**, *11*, No. 2003752.

(18) González, M. A.; Aoun, B.; Price, D. L.; Izaola, Z.; Russina, M.; Ollivier, J.; Saboungi, M.-L. Molecular Dynamics in 1-Alkyl-3-Methylimidazolium Bromide Ionic Liquids: A Reanalysis of Quasielastic Neutron Scattering Results. *AIP Conf. Proc.* **2018**, *1969*, No. 20002.

(19) Jafta, C. J.; Bridges, C.; Haupt, L.; Do, C.; Sippel, P.; Cochran, M. J.; Krohns, S.; Ohl, M.; Loidl, A.; Mamontov, E.; et al. Ion Dynamics in Ionic-Liquid-Based Li-Ion Electrolytes Investigated by Neutron Scattering and Dielectric Spectroscopy. *ChemSusChem* **2018**, *11*, 3512−3523.

(20) Nemoto, F.; Kofu, M.; Nagao, M.; Ohishi, K.; Takata, S.; Suzuki, J.; Yamada, T.; Shibata, K.; Ueki, T.; Kitazawa, Y.; et al. Neutron Scattering Studies on Short- and Long-Range Layer Structures and Related Dynamics in Imidazolium-Based Ionic Liquids. *J. Chem. Phys.* **2018**, *149*, 054502.

(21) Kofu, M.; Tyagi, M.; Inamura, Y.; Miyazaki, K.; Yamamuro, O. Quasielastic Neutron Scattering Studies on Glass-Forming Ionic Liquids with Imidazolium Cations. *J. Chem. Phys.* **2015**, *143*, No. 234502.

(22) Burankova, T.; Mora Cardozo, J. F.; Rauber, D.; Wildes, A.; Embs, J. P. Linking Structure to Dynamics in Protic Ionic Liquids: A Neutron Scattering Study of Correlated and Single-Particle Motions. *Sci. Rep.* **2018**, *8*, No. 16400.

(23) Lundin, F.; Hansen, H. W.; Adrjanowicz, K.; Frick, B.; Rauber, D.; Hempelmann, R.; Shebanova, O.; Niss, K.; Matic, A. Pressure and Temperature Dependence of Local Structure and Dynamics in an Ionic Liquid. *J. Phys. Chem. B* **2021**, *125*, 2719−2728.

(24) Lundin, F.; Falus, P.; Matic, A. Influence of HFE on the Dynamics of an Ionic Liquid Electrolyte *Institute Laue-Langevin (ILL)*, 2021, https://doi.org/10.5291/ILL-DATA.6-02-618.

(25) Fouquet, P.; Ehlers, G.; Farago, B.; Pappas, C.; Mezei, F. The Wide-Angle Neutron Spin Echo Spectrometer Project WASP. *J. Neutron Res.* **2007**, *15*, 39−47.

(26) Xu, X.; Liu, Y.; Hwang, J. Y.; Kapitanova, O. O.; Song, Z.; Sun, Y. K.; Matic, A.; Xiong, S. Role of Li-Ion Depletion on Electrode Surface: Underlying Mechanism for Electrodeposition Behavior of Lithium Metal Anode. *Adv. Energy Mater.* **2020**, *10*, No. 2002390.

(27) Martinelli, A.; Matic, A.; Jacobsson, P.; Börjesson, L.; Fernicola, A.; Scrosati, B. Phase Behavior and Ionic Conductivity in Lithium Bis(Trifluoromethanesulfonyl)Imide-Doped Ionic Liquids of the

Pyrrolidinium Cation and Bis(Trifluoromethanesulfonyl)Imide Anion. *J. Phys. Chem. B* **2009**, *113*, 11247−11251.
(28) Pitawala, J.; Kim, J. K.; Jacobsson, P.; Koch, V.; Croce, F.; Matic, A. Phase Behaviour, Transport Properties, and Interactions in Li-Salt Doped Ionic Liquids. *Faraday Discuss.* **2012**, *154*, 71−80.
(29) Gao, X.; Wu, F.; Mariani, A.; Passerini, S. Concentrated Ionic-Liquid-Based Electrolytes for High-Voltage Lithium Batteries with Improved Performance at Room Temperature. *ChemSusChem* **2019**, *12*, 4185−4193.
(30) Wang, Y.; Chen, W.; Zhao, Q.; Jin, G.; Xue, Z.; Wang, Y.; Mu, T. Ionicity of Deep Eutectic Solvents by Walden Plot and Pulsed Field Gradient Nuclear Magnetic Resonance (PFG-NMR. *Phys. Chem. Chem. Phys.* **2020**, *22*, 25760−25768.
(31) MacFarlane, D. R.; Forsyth, M.; Izgorodina, E. I.; Abbott, A. P.; Annat, G.; Fraser, K. On the Concept of Ionicity in Ionic Liquids. *Phys. Chem. Chem. Phys.* **2009**, *11*, 4962−4967.
(32) Girard, G. M. A.; Hilder, M.; Zhu, H.; Nucciarone, D.; Whitbread, K.; Zavorine, S.; Moser, M.; Forsyth, M.; MacFarlane, D. R.; Howlett, P. C. Electrochemical and Physicochemical Properties of Small Phosphonium Cation Ionic Liquid Electrolytes with High Lithium Salt Content. *Phys. Chem. Chem. Phys.* **2015**, *17*, 8706−8713.
(33) Triolo, A.; Russina, O.; Fazio, B.; Appetecchi, G. B.; Carewska, M.; Passerini, S. Nanoscale Organization in Piperidinium-Based Room Temperature Ionic Liquids. *J. Chem. Phys.* **2009**, *130*, No. 164521.
(34) Aguilera, L.; Völkner, J.; Labrador, A.; Matic, A. The Effect of Lithium Salt Doping on the Nanostructure of Ionic Liquids. *Phys. Chem. Chem. Phys.* **2015**, *17*, 27082−27087.
(35) Fujii, K.; Hamano, H.; Doi, H.; Song, X.; Tsuzuki, S.; Hayamizu, K.; Seki, S.; Kameda, Y.; Dokko, K.; Watanabe, M.; Umebayashi, Y. Unusual Li+ Ion Solvation Structure in Bis-(Fluorosulfonyl)Amide Based Ionic Liquid. *J. Phys. Chem. C* **2013**, *117*, 19314−19324.
(36) Carstens, T.; Lahiri, A.; Borisenko, N.; Endres, F. [Py1,4]FSI-NaFSI-Based Ionic Liquid Electrolyte for Sodium Batteries: Na+ Solvation and Interfacial Nanostructure on Au(111). *J. Phys. Chem. C* **2016**, *120*, 14736−14741.
(37) Pitawala, J.; Martinelli, A.; Johansson, P.; Jacobsson, P.; Matic, A. Coordination and Interactions in a Li-Salt Doped Ionic Liquid. *J. Non-Cryst. Solids* **2015**, *407*, 318−323.
(38) Solano, C. J. F.; Jeremias, S.; Paillard, E.; Beljonne, D.; Lazzaroni, R. A Joint Theoretical/Experimental Study of the Structure, Dynamics, and Li+ Transport in Bis([Tri]Fluoro-[Methane]Sulfonyl)Imide [T]FSI-Based Ionic Liquids. *J. Chem.Phys.* **2013**, *139*, No. 034502.
(39) Telling, M. T. F. *A Practical Guide to Quasi-Elastic Neutron Scattering*; Royal Society of Chemistry, 2020.
(40) Kofu, M.; Faraone, A.; Tyagi, M.; Nagao, M.; Yamamuro, O. Two Inherent Crossovers of the Diffusion Process in Glass-Forming Liquids. *Phys. Rev. E* **2018**, *98*, 42601.

https://doi.org/10.1021/acs.jpcc.2c04503
J. Phys. Chem. C 2022, 126, 16262−16271